Short-range-ordering strengthening and the evolution of dislocation-nucleation modes in an $Fe_{40}Mn_{20}Cr_{20}Ni_{20}$ high-entropy alloy

Q. Zhang [a], P.K. Liaw [b], and J.W. Qiao [a,*]

[a] Laboratory of High-Entropy Alloys, College of Materials Science and Engineering, Taiyuan University of Technology, Taiyuan, 030024, China

[b] Department of Materials Science and Engineering, The University of Tennessee, Knoxville, TN, 37996-2200, USA

Abstract

Compared with the $Fe_{40}Mn_{20}Cr_{20}Ni_{20}$ high-entropy alloy in an homogenized state, it has higher incipient plastic strength after high-temperature aging, which is attributed to the generation of short-range orderings (SROs) caused by the local composition fluctuations. Based on nanoindentation results at different loading rates, the evolution trends of homogeneous and heterogeneous dislocation-nucleation modes under the effect of SROs are revealed for the first time. Under the action of the high-solution friction stress, which is caused by the high loading rate, and coherency-strain field, which is caused by SROs, the critical shear stress of the dislocation nucleation increases. Furthermore, with the increase of the loading rate, the probability of heterogeneous nucleation in homogenized samples increases, while that in aged samples is the opposite. From the perspective of the distribution of dislocation-nucleation sites, this opposite trend can be well explained by assuming the spreading resistance of an activatable region. In short, the present work reveals the pivotal role of SROs on dislocation-nucleation modes and paves the way for the quantitative study concerning SROs and their strengthening effects.

Keywords: High-entropy alloys; Short-range orderings; Incipient plasticity; Loading rate; Coherency-strain-field strengthening.

* Corresponding author. E-mail: qiaojunwei@gmail.com (J.W. Qiao)

As a new generation of structural materials, high-entropy alloys (HEAs) were originally proposed in the form of a single-phase ideal solid solution. Due to the interaction of multiple principal elements, however, the HEAs are bound to be different from the traditional alloys in their structures. Issued from the atomic scale, complex interactions among diverse constituents can trigger local fluctuations of chemical compositions, resulting in the emergence of chemical short-range orderings (SROs). To date, the unambiguous evidence of SROs has been experimentally exhibited in a few HEAs [1-8]. Moreover, it is confirmed that the presence of SROs plays a significant role in the deformation mechanisms of alloys, which is closely related to the nucleation and movement of dislocations [7, 9-16]. But unfortunately, the strengthening mechanism of SROs has been the yet hitherto pending question, full of challenges especially when focusing on the micro level.

Considering that SROs are essentially heterogeneous distributions of components on the nanoscale, it is extremely difficult to detect its microscopic reinforcement mechanism. In this regard, incipient plasticity, detected by a nanoindentation technique, has been corroborated to be capable of detecting the effect of SROs [2, 9]. Here, the incipient plasticity, that is, the elastic-plastic transformation behavior, is shown as the first pop-in event on the load-displacement (*P*-*h*) curve [17, 18]. For the alloys in a fully annealed state, the first pop-in event is dominated by dislocation nucleation [19]. Recently, the bimodality of the incipient plastic strength of crystalline materials has been proposed: concomitantly, two dislocation-nucleation mechanisms, homogeneous nucleation and heterogeneous nucleation, are separated and discussed [9]. Combining with the evolution of the dislocation-nucleation mechanism, the pivotal role of SROs progressively comes to light, but nonetheless has numerous queries regarding the reinforcement process. In light of the aforementioned content, our work is devoted to exploring the strengthening way of SROs by adjusting the loading rate.

In the present work, non-equiatomic $Fe_{40}Mn_{20}Cr_{20}Ni_{20}$ HEAs were selected for subsequent studies for their superior application prospects [20]. Firstly, alloy ingots were prepared by arc-melting under a high-purity argon atmosphere, and the purity of

each raw material was at least 99.9 weight percent (wt %). It should be noted that an additional 5 wt % Mn was added to compensate for the evaporation of Mn during melting. To ensure chemical homogeneity, the ingots were flipped and remelted at least four times, followed by drop casting into a rectangular plate with a thickness of 6 mm. As-cast $Fe_{40}Mn_{20}Cr_{20}Ni_{20}$ ingots were hot-rolled at 900 ◦C for a 50%-thickness reduction. Afterwards, the rolled plates were encapsulated in a quartz tube and filled with high-purity argon, and then homogenized at 1,200 ◦C for 24 h, followed by water-quenching to suppress SROs formation. Finally, partial specimens were aged at 1,050 ℃ for 12h, followed by furnace-cooling. At this time, the local fluctuations of chemical compositions become obvious, which leads to the generation of SROs. On this basis, the nanoindentation tests were carried out on the homogenized and aged samples to research the effect of SROs. From here on, the samples in the homogenized state and aging states are described by HS and AS, respectively. In particular, all mechanically polished samples need to be electropolished before nanoindentation experiments to remove any work-hardened surface layer. Here, a solution of 75% methanol and 25% nitric acid in volume percent was used.

The phase structures and lattice parameters were characterized by X-ray diffraction (XRD, PANalytical AERIS). The microstructure was confirmed by optical microscopy. The incipient plasticity tests were performed by a nanoindentation instrument (Bruker, Minneapolis, MN, USA) with a Berkovich tip. And the tip radius was calibrated on a reference fused quartz sample with a value of ~ 245 nm. Nanoindentation tests were conducted with a fixed maximum load of 200 μN, and three loading rates of 20 μN/s, 80 μN/s, and 200 μN/s, respectively. Under each test condition, more than 200 tests were performed on each sample with a 5-μm interval. To eliminate the influence of the grain boundary, all tests were conducted in the grain far away from the grain boundary.

Figure 1 exhibits the XRD patterns and microstructure images of homogenized and aged $Fe_{40}Mn_{20}Cr_{20}Ni_{20}$ HEAs, and a single face-centered-cubic (FCC) structure is suggested, which implies no distinct new phase formation after aging. The equiaxed crystal sizes of all samples are close to 200 μm, which is conducive to the

nanoindentation tests. From HS to AS, the lattice constant, a, of the alloy changes slightly from ~ 3.62 Å to ~ 3.61 Å. On the representative P-h curve, obtained by the indentation test, the elastic segment before the first pop-in can be well depicted by the Hertzian contact framework [21, 22]:

$$P = \frac{4}{3} E_{\mathrm{r}} \sqrt{R h^3} \tag{1}$$

where R is the tip radius of the indenter, E_{r} is the reduced modulus, which can be determined by: $E_{\mathrm{r}} = [(1 - v_i^2)/E_i + (1 - v_s^2)/E_s]^{-1}$. Thereinto, v is Poisson's ratio, E is Young's modulus, and the subscripts, i and s, stand for the indenter and samples, respectively. Whereafter, based on the statistics of more than 200 P-$h^{3/2}$ pairs at the first pop-in of HS and AS samples with various loading rates, as demonstrated in Fig. 2, the E_{r} can be derived from the slope of linear fitting as ~ 196 GPa. Combined with v_{s}, measured by an ultrasonic pulse-echo technique [2], the elastic moduli, E, and the shear moduli, G, are calculated as ~ 217 and ~ 84 GPa, respectively.

For HS and AS samples, the incipient plasticity arises from the dislocation nucleation, and its critical shear stress, $\tau_{\max}$, is expressed as [21]:

$$\tau_{\max} = \frac{0.47}{\pi} \left(\frac{4E_{\mathrm{r}}}{3R} \right)^{2/3} P^{1/3} \tag{2}$$

The statistical histograms of $\tau_{\max}$ for HS and AS are presented in Fig. 3. It is intuitive that the distributions of $\tau_{\max}$ are not completely symmetrical, which has been also explained in the previous work [11]. To gain insights into the possible source of this asymmetry, the Kernel density estimates (KDEs) of the histograms are executed [23, 24], and the obtained KDE curves are deconvoluted, based on a Gaussian statistical model [9, 25]:

$$f(\tau_{\max}) = \frac{1}{\sigma\sqrt{2\pi}} exp\left(-\frac{(\tau_{\max} - \overline{\tau_{\max}})^2}{2\sigma^2} \right) \tag{3}$$

where σ is the standard deviation. In Fig. 3, the deconvolution results confirm a bimodal distribution of $\tau_{\max}$, and low-intensity and high-intensity peaks are named as Peaks 1 and 2, respectively. Relevant parameters of Peaks 1 and 2, such as the mean ($\overline{\tau_{\max}}$), ratio to shear modulus ($\overline{\tau_{\max}}$/G), and areal fraction (AF) of each peak, are listed in Table 1. As far as we know, the deconvolution peaks, i.e., low-intensity and high-intensity peaks, are dominated by disparate dislocation-nucleation mechanisms. For further

information, the activation volume, V, corresponding to each peak is derived from its relationship with the cumulative probability, F, of τ_{max} [26, 27]:

$$\ln[-\ln(1-F)] = \frac{V}{kT}\tau_{\max} + \beta \tag{4}$$

where k is the Boltzmann constant, T is the absolute temperature, and the parameter, β, is of a weak P dependence. The calculation results are annotated with the same color near the corresponding peaks in Fig. 3.

As for the dislocation-nucleation mechanisms, homogeneous nucleation requires a higher critical shear stress, compared to heterogeneous nucleation [28-30]. Hence, Peaks 1 and 2 are dominated by heterogeneous and homogeneous nucleation mechanisms, respectively. In addition, the results show that the activation volume of the homogeneous nucleation, which is suggested to be no larger than 1 Ω, is all less than or equal to that of the heterogeneous nucleation. This phenomenon was also mentioned in previous reports [9, 19].

Focusing on the evolution law of the τ_{max} for Peaks 1 and 2, it can be found that SROs generation gives rise to an elevation of τ_{max}, and the increase in the loading rate also leads to a consistent trend [31, 32]. Besides, the probability of two nucleation manners of dislocations, denoted by the AF of each peak, also changes with a shift in τ_{max}. Of special note is that the AF values of the two peaks for HS and AS samples show opposite trends. The specific analysis is carried out in the following.

The nucleation of dislocations in a perfect crystal lattice is homogenous. On the contrary, those assisted by defects are heterogeneous. At this point, a deep connection exists between the defect type and the probability of the heterogeneous nucleation. Therefore, nucleation-site densities, ρ, of different nucleation mechanisms are discussed. If we consider a Poisson distribution of nucleation sites among the highly stressed zone under the indenter, the probabilities of different nucleation modes, P, can be depicted as [23]:

$$P = 1 - exp(-\rho V_s) \tag{5}$$

where P is the AF of the peak, and V_s is the volume of the highly stressed zone. According to the assumption of Mason et al. [17], V_s is calculated as: $V_s = \pi a_c^3$, where

a_c is the contact radius. For the quite shallow depth when the initial plasticity takes place, the contact part between the indenter and the sample surface can be approximately spherical, at this time, $a_c = \left(\frac{3PR}{4E_r}\right)^{1/3}$ [33]. On the above basis, the nucleation-site densities, ρ, can be calculated. Furthermore, the average interval of nucleation sites can also be obtained from: $l = 1/\sqrt[3]{\rho_{low}}$ [11]. The corresponding calculation results of each peak are marked in Table 1. For the heterogeneous nucleation, the nucleation-site distances are estimated to be ~ 46.7 – 104.0 nm. In conjugation with the density of various defects, when the alloy is in a thermal equilibrium at room temperature, the heterogeneous nucleation of dislocations is most likely assisted by vacancies. Here, the average vacancy spacing of $Fe_{40}Mn_{20}Cr_{20}Ni_{20}$ is ~ 23 nm [18]. For the diversity of the heterogeneous nucleation-site distance and the vacancy spacing, the influence of SROs, as well as the heterogeneity of the stress field under the indenter should be considered.

Driven by the higher loading rate, the $\overline{\tau_{max}}$ of all peaks goes up, as such the variation of the solution-friction stress of the alloys must be considered. In terms of a classical dislocation-dynamics model, the friction stress, σ_0, due to the solid solution, can be expressed as a function of the strain rate, $\dot{\varepsilon}$ [34]:

$$\sigma_0 = Al n\dot{\varepsilon} + B \tag{6}$$

where $A = \frac{MkT}{\Delta V_s}$, and $B = \frac{M}{\Delta V_s}(\Delta G_S - kT \ln \frac{\rho_m b \kappa v_0}{M})$. For the HS samples, the increase of the shear stress for dislocation nucleation at high loading rates is mainly caused by the increase of the solution-friction stress. Within the loading rate range in this paper, the increments of the mean τ_{max} of Peaks 1 and 2 reaches ~ 0.14 GPa and ~ 0.15 GPa, respectively. However, for the tests of AS samples at different loading rates, the solution friction stress and SROs both contribute to the increase of the shear stress for dislocation nucleation.

So far, the research on SROs is still lacking, and the reason why the dislocation nucleation is strengthened has not been reported. When it comes to the enhancement effect of SROs, two factors are involved, including the coherency-strain-field strengthening and precipitation strengthening arising from the energy required to

produce an anti-phase boundary (APB) by dislocations-shearing SROs [35]. In consideration of the nucleation process of dislocations, the shearing of SROs is not involved, that is, the precipitation strengthening has not yet worked. Therefore, it is the coherent-strain-field strengthening that increases the dislocation-nucleation strength of AS samples. Because of the tiny size of SROs, which can be described as [36, 37]:

$$\Delta\tau = 4.1G\varepsilon^{3/2}\left(\frac{rf}{b}\right)^{1/2} \tag{7}$$

where ε is the lattice mismatch between the SROs and matrix, b is the Burgers vector, r and f are the radius and volume fraction of SROs, respectively. Based on Eq. (7), the relationship between the coherent-strain-field strengthening and related parameters of SROs has been explained. It is imperative to draw insights into the quantitative study of SROs, and the present work will lend credence to this goal.

According to the distribution situation of the dislocation-nucleation strength of the two samples in Fig. 3, it is obvious that the dislocation nucleation of HS samples is dominated by the homogeneous nucleation, while that of AS samples is dominated by the heterogeneous nucleation [9, 11]. The change of the dominant nucleation mechanism is attributed to the increase of τ_{max} caused by SROs. That is to say, in AS samples, compared with the high τ_{max} required for the homogeneous nucleation, expressed by τ_{max} of Peaks 2, the τ_{max} of the heterogeneous nucleation under the indenter is easier to reach. Besides, after increasing the loading rate, the elevation of the solution-friction stress causes that the τ_{max} of the dislocation-nucleation rises [34]. Concomitantly, an opposite fluctuation trend for the AF of different peaks appears, between HS and AS samples. Specifically, when the loading rate changes from 20 μN/s to 800 μN/s, the AF of Peak 1 for HS samples changes from 0.09 to 0.23, which for AS samples changes from 0.70 to 0.57. This phenomenon can be analyzed from the perspective of the nucleation-site distribution under the indenter.

Under the joint action of the loading rate and SROs, the probabilities of different nucleation mechanisms show a complex evolvement rule. In Fig. 4, a schematic diagram of the distribution and evolution of heterogeneous-nucleation sites under the indenter is shown. Before the SRO generation, from (a) to (b) in Fig. 4, with

increasing the loading rate, τ_{max} of the homogeneous nucleation gradually becomes difficult to achieve. Hence, the probability of the heterogeneous nucleation rises. From the perspective of nucleation sites, the higher τ_{max}, that is, the larger critical load, which expands the highly stressed zone. At this time, the number of vacancies in V_s goes up, and the stress at more vacancies reaches the critical value. As a result, more vacancies become nucleation sites for the heterogeneous nucleation, and the calculated density of heterogeneous nucleation sites, ρ_{low}, increases.

After aging, in the highly stressed zone, the addition of the SROs' coherent-strain field makes the nucleation situation more complicated. From (c) to (d) in Fig. 4, the highly stressed zone expands, and more vacancies are included. For convenience, an activatable area is assumed here, whose size is determined by the heterogeneous-nucleation site farthest from the center of the highly stressed zone. In AS samples, the spreading resistance of the activatable region, τ_{exp}, is determined by the combined action of the solution-friction stress and coherent-strain-field strengthening. Because of the gradient distribution of the stress in the highly stressed zone [33, 38], dislocation nucleation can only occur when the shear stress at the vacancy is higher than τ_{exp}. As presented in Fig. 4(c), the shear stress at the farthest activatable vacancy (named vacancy X) that can cause heterogeneous nucleation should be higher than τ_{exp}. With the increase of the loading rate, a strong lattice friction leads to higher τ_{max} and τ_{exp}. Accordingly, the critical load of heterogeneous nucleation increases, and the relative test depth and highly stressed zone become larger. However, at this time, the shear stress at the vacancy, which is farther from the center of the highly stressed zone than vacancy X may still be less than τ_{exp}. Eventually, in AS samples, the density of heterogeneous-nucleation sites, ρ_{low}, in the highly stressed zone slightly decreases with the increase of the loading rate.

To date, the significant strengthening effect of SROs on the incipient plasticity has been proposed, but the specific strengthening mode and its evolution have not been mentioned. In the present work, high-temperature aging is used to promote the formation of SROs, which stems from the more obvious atomic-site preferences. And then the evolution process of dislocation-nucleation modes is studied, by designing

nanoindentation tests at different loading rates. The results show that compared with the effect of the loading rate on the incipient plasticity, the strengthening induced by the generation of SROs are more notable. For the opposite evolution trend of the heterogeneous nucleation probability in HS and AS samples, the spreading resistance of the activatable region, τ_{exp}, is defined here, which is represented by the joint action of the solution-friction stress and the coherent strain-field strengthening. On the above basis, the pivotal influence of SROs on the dislocation-nucleation modes is becoming clear, which not only provides a new idea for the SRO detection, but also lends credence to the quantitative examination of SRO strengthening.

Acknowledge

The authors would like to acknowledge the financial support of the National Natural Science Foundation of China (No. 52271110), and Key Research and Development Program of Shanxi Province (No. 202102050201008). PKL very much appreciates the supports from (1) the National Science Foundation (DMR – 1611180, 1809640, and 2226508) and (2) the Army Research Office (W911NF-13–1-0438 and W911NF-19–2-0049).

References

[1] Q. Ding, Y. Zhang, X. Chen, X. Fu, D. Chen, S. Chen, L. Gu, F. Wei, H. Bei, Y. Gao, M. Wen, J. Li, Z. Zhang, T. Zhu, R.O. Ritchie, Q. Yu, Tuning element distribution, structure and properties by composition in high-entropy alloys, Nature 574(7777) (2019) 223-227.

[2] R. Zhang, S. Zhao, J. Ding, Y. Chong, T. Jia, C. Ophus, M. Asta, R.O. Ritchie, A.M. Minor, Short-range order and its impact on the CrCoNi medium-entropy alloy, Nature 581(7808) (2020) 283-287.

[3] X. Chen, Q. Wang, Z. Cheng, M. Zhu, H. Zhou, P. Jiang, L. Zhou, Q. Xue, F. Yuan, J. Zhu, X. Wu, E. Ma, Direct observation of chemical short-range order in a medium-entropy alloy, Nature 592(7856) (2021) 712-716.

[4] D. Liu, Q. Wang, J. Wang, X.F. Chen, P. Jiang, F.P. Yuan, Z.Y. Cheng, E. Ma, X.L. Wu, Chemical short-range order in $Fe_{50}Mn_{30}Co_{10}Cr_{10}$ high-entropy alloy, Materials Today Nano 16 (2021) 100139.

[5] L.J. Santodonato, Y. Zhang, M. Feygenson, C.M. Parish, M.C. Gao, R.J.K. Weber, J.C. Neuefeind, Z. Tang, P.K. Liaw, Deviation from high-entropy configurations in the atomic distributions of a multi-principal-element alloy, Nat. Commun. 6 (2015) 5964.

[6] Y. Ma, Q. Wang, C. Li, L.J. Santodonato, M. Feygenson, C. Dong, P.K. Liaw, Chemical short-range orders and the induced structural transition in high-entropy alloys, Scr. Mater. 144 (2018) 64-68.

[7] H.-W. Hsiao, R. Feng, H. Ni, K. An, J.D. Poplawsky, P.K. Liaw, J.-M. Zuo, Data-driven electron-diffraction approach reveals local short-range ordering in CrCoNi with ordering effects, Nat. Commun. 13(1) (2022) 6651-6651.

[8] M. Zhang, Q. Yu, C. Frey, F. Walsh, M.I. Payne, P. Kumar, D. Liu, T.M. Pollock, M.D. Asta, R.O. Ritchie, A.M. Minor, Determination of peak ordering in the CrCoNi medium-entropy alloy via nanoindentation, Acta Mater. 241 (2022) 118380.

[9] Y. Zhao, J.-M. Park, J.-I. Jang, U. Ramamurty, Bimodality of incipient plastic strength in face-centered cubic high-entropy alloys, Acta Materialia 202 (2021)

124-134.

[10] X. Yang, Y. Xi, C. He, H. Chen, X. Zhang, S. Tu, Chemical short-range order strengthening mechanism in CoCrNi medium-entropy alloy under nanoindentation, Scripta Materialia 209 (2022) 114364.

[11] Q. Zhang, X. Jin, X.H. Shi, J.W. Qiao, P.K. Liaw, Short range ordering and strengthening in CoCrNi medium-entropy alloy, Materials Science and Engineering a-Structural Materials Properties Microstructure and Processing 854 (2022) 143890.

[12] E. Antillon, C. Woodward, S.I. Rao, B. Akdim, T.A. Parthasarathy, Chemical short range order strengthening in a model FCC high entropy alloy, Acta Materialia 190 (2020) 29-42.

[13] Q.-J. Li, H. Sheng, E. Ma, Strengthening in multi-principal element alloys with local-chemical-order roughened dislocation pathways, Nature Communications 10 (2019) 3563.

[14] S. Chen, Z.H. Aitken, S. Pattamatta, Z. Wu, Z.G. Yu, D.J. Srolovitz, P.K. Liaw, Y.-W. Zhang, Simultaneously enhancing the ultimate strength and ductility of high-entropy alloys via short-range ordering, Nat. Commun. 12(1) (2021) 4953.

[15] S. Chen, Z.H. Aitken, S. Pattamatta, Z. Wu, Z.G. Yu, R. Banerjee, D.J. Srolovitz, P.K. Liaw, Y.-W. Zhang, Chemical-affinity disparity and exclusivity drive atomic segregation, short-range ordering, and cluster formation in high-entropy alloys, Acta Mater. 206 (2021) 116638.

[16] O. Rodriguez de la Fuente, J.A. Zimmerman, M.A. Gonzalez, J. de La Figuera, J.C. Hamilton, W.W. Pai, J.M. Rojo, Dislocation emission around nanoindentations on a (001) fcc metal surface studied by scanning tunneling microscopy and atomistic simulations, Phys. Rev. Lett. 88(3) (2002) 036101-036101.

[17] J.K. Mason, A.C. Lund, C.A. Schuh, Determining the activation energy and volume for the onset of plasticity during nanoindentation, Physical Review B 73(5) (2006) 054102.

[18] C. Zhu, Z.P. Lu, T.G. Nieh, Incipient plasticity and dislocation nucleation of FeCoCrNiMn high-entropy alloy, Acta Materialia 61(8) (2013) 2993-3001.

[19] K. Gan, D. Yan, S. Zhu, Z. Li, Interstitial effects on the incipient plasticity and

dislocation behavior of a metastable high-entropy alloy: Nanoindentation experiments and statistical modeling, Acta Materialia 206 (2021) 116633.

[20] J.C. Cheng, J. Xu, X.J. Zhao, K.W. Shi, J. Li, Q. Zhang, J.W. Qiao, J.Y. Huang, S.N. Luo, Shock compression and spallation of a medium-entropy alloy $Fe_{40}Mn_{20}Cr_{20}Ni_{20}$, Materials Science and Engineering a-Structural Materials Properties Microstructure and Processing 847 (2022).

[21] K.L. Johnson, Contact Mechanics, Cambridge University Press (1985).

[22] L. Zhang, T. Ohmura, Plasticity Initiation and Evolution during Nanoindentation of an Iron-3% Silicon Crystal, Phys. Rev. Lett. 112(14) (2014) 145504.

[23] J.H. Perepezko, S.D. Imhoff, M.W. Chen, J.Q. Wang, S. Gonzalez, Nucleation of shear bands in amorphous alloys, Proceedings of the National Academy of Sciences of the United States of America 111(11) (2014) 3938-3942.

[24] S. Nag, R.L. Narayan, J.-i. Jang, C. Mukhopadhyay, U. Ramamurty, Statistical nature of the incipient plasticity in amorphous alloys, Scripta Materialia 187 (2020) 360-365.

[25] Y. Gao, H. Bei, Strength statistics of single crystals and metallic glasses under small stressed volumes, Progress in Materials Science 82 (2016) 118-150.

[26] Y.X. Ye, Z.P. Lu, T.G. Nieh, Dislocation nucleation during nanoindentation in a body-centered cubic TiZrHfNb high-entropy alloy, Scripta Materialia 130 (2017) 64-68.

[27] G. Yang, Y. Zhao, D.-H. Lee, J.-M. Park, M.-Y. Seok, J.-Y. Suh, U. Ramamurty, J.-l. Jang, Influence of hydrogen on incipient plasticity in CoCrFeMnNi high-entropy alloy, Scripta Materialia 161 (2019) 23-27.

[28] T.A. Michalske, J.E. Houston, Dislocation nucleation at nano-scale mechanical contacts, Acta Mater. 46(2) (1998) 391-396.

[29] Y.L. Chiu, A.H.W. Ngan, Time-dependent characteristics of incipient plasticity in nanoindentation of a Ni_3Al single crystal, Acta Mater. 50(6) (2002) 1599-1611.

[30] C.A. Schuh, J.K. Mason, A.C. Lund, Quantitative insight into dislocation nucleation from high-temperature nanoindentation experiments, Nature Materials 4(8) (2005) 617-621.

[31] C.A. Schuh, A.C. Lund, Application of nucleation theory to the rate dependence of incipient plasticity during nanoindentation, J. Mater. Res. 19(7) (2004) 2152-2158.

[32] Y. Wang, W. Liu, Y. Ma, Y. Huang, Y. Tang, H. Luo, Q. Yu, Indentation depth dependent micromechanical properties and rate dependent pop-in events of $(Au,Cu)_5Sn$, Materials Letters 131 (2014) 57-60.

[33] J.R. Morris, H. Bei, G.M. Pharr, E.P. George, Size effects and stochastic behavior of nanoindentation pop in, Phys. Rev. Lett. 106(16) (2011) 165502.

[34] Z.Y. Liang, X. Wang, W. Huang, M.X. Huang, Strain rate sensitivity and evolution of dislocations and twins in a twinning-induced plasticity steel, Acta Mater. 88 (2015) 170-179.

[35] S. Dasari, A. Jagetia, A. Sharma, M.S.K.K.Y. Nartu, V. Soni, B. Gwalani, S. Gorsse, R. Banerjee, Tuning the degree of chemical ordering in the solid solution of a complex concentrated alloy and its impact on mechanical properties, Acta Materialia 212 (2021) 116938.

[36] Z. Guo, W. Sha, Quantification of precipitation hardening and evolution of precipitates, Mater. Trans. 43(6) (2002) 1273-1282.

[37] G. T., Precipitation hardening in metals, Mater. Sci. Technol. 15(1) (1999) 30-36.

[38] D. Wu, J.R. Morris, T.G. Nieh, Effect of tip radius on the incipient plasticity of chromium studied by nanoindentation, Scripta Materialia 94 (2015) 52-55.

Table 1

The results of deconvolution by the Gaussian distribution and the related parameters of dislocation-nucleation sites.

Sample		Peak	$\overline{\tau_{\max}}$ (GPa)	$\overline{\tau_{\max}}/G$	AF	ρ (μm^{-3})	l (nm)
HS	20 μN/s	1	5.16	1/16	0.09	0.89×10^3	104.0
		2	6.05	1/14	0.91	14.08×10^3	41.4
	80 μN/s	1	5.25	1/16	0.11	1.04×10^3	98.7
		2	6.13	1/14	0.89	12.47×10^3	43.1
	200 μN/s	1	5.30	1/16	0.23	2.27×10^3	76.1
		2	6.20	1/14	0.77	7.94×10^3	50.1
AS	20 μN/s	1	5.41	1/15	0.70	9.79×10^3	46.7
		2	6.25	1/13	0.30	1.90×10^3	80.8
	80 μN/s	1	5.63	1/15	0.68	8.26×10^3	49.5
		2	6.35	1/13	0.32	1.95×10^3	80.1
	200 μN/s	1	5.67	1/15	0.57	5.94×10^3	55.2
		2	6.39	1/13	0.43	2.77×10^3	71.1

.

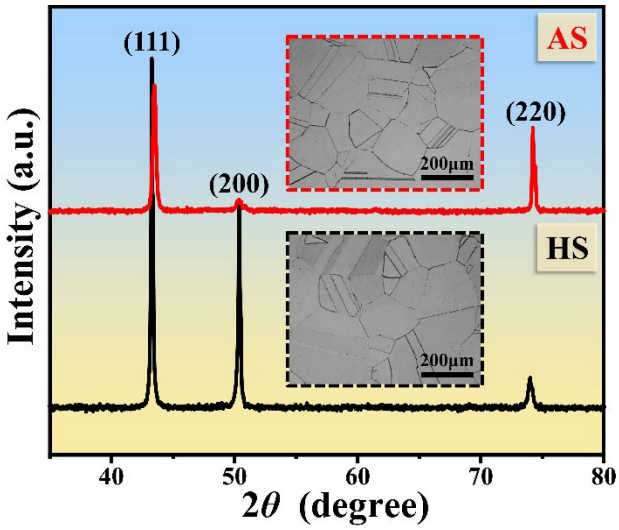

Fig. 1. XRD patterns of homogenized and aged samples. Microstructure images are marked with the same color-dotted border near the XRD curves.

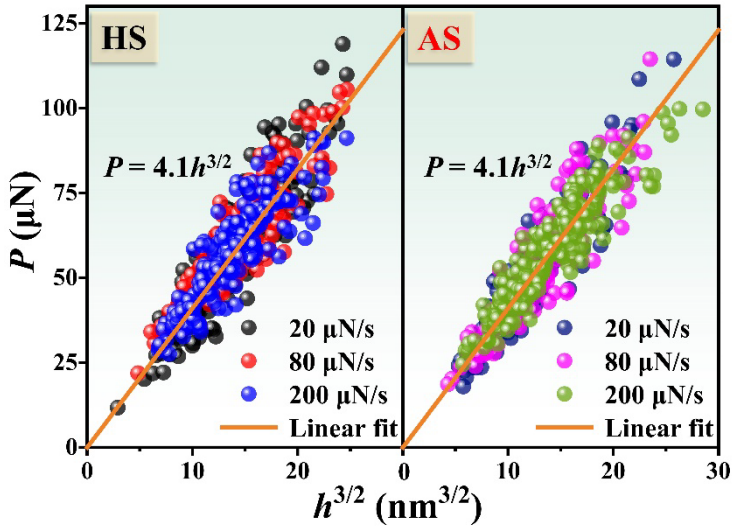

Fig. 2. Statistics of at least 200 P-$h^{3/2}$ pairs at the first pop-in of homogenized and aged samples under various loading conditions.

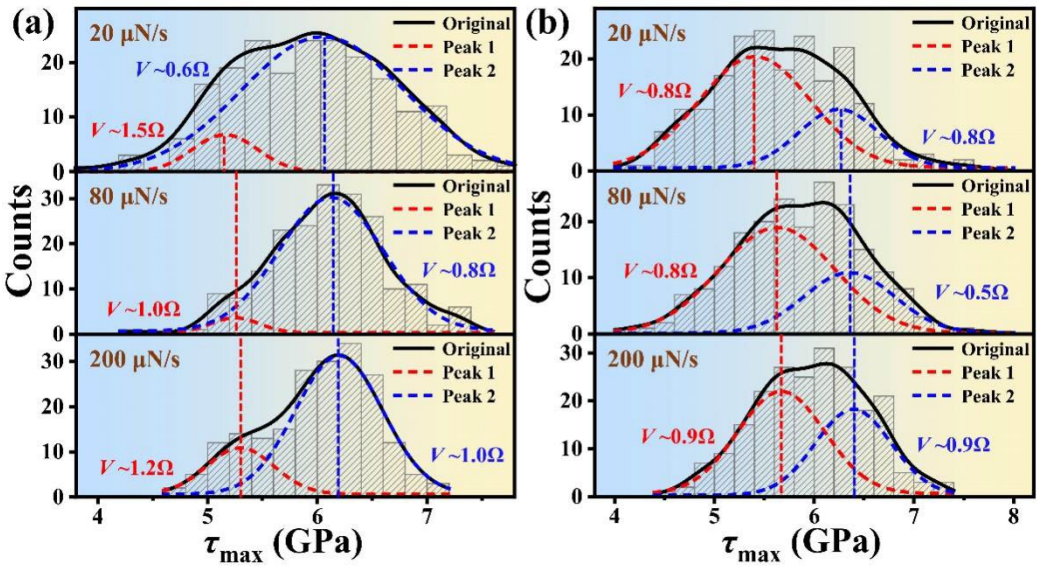

Fig. 3. Histograms, KDE curves and deconvolution results by Gaussian distributions for the tests of (a) homogenized and (b) aged samples. The V of each peak is also given in terms of Ω, and the dashed line marks the average τ_{max} value of each peak

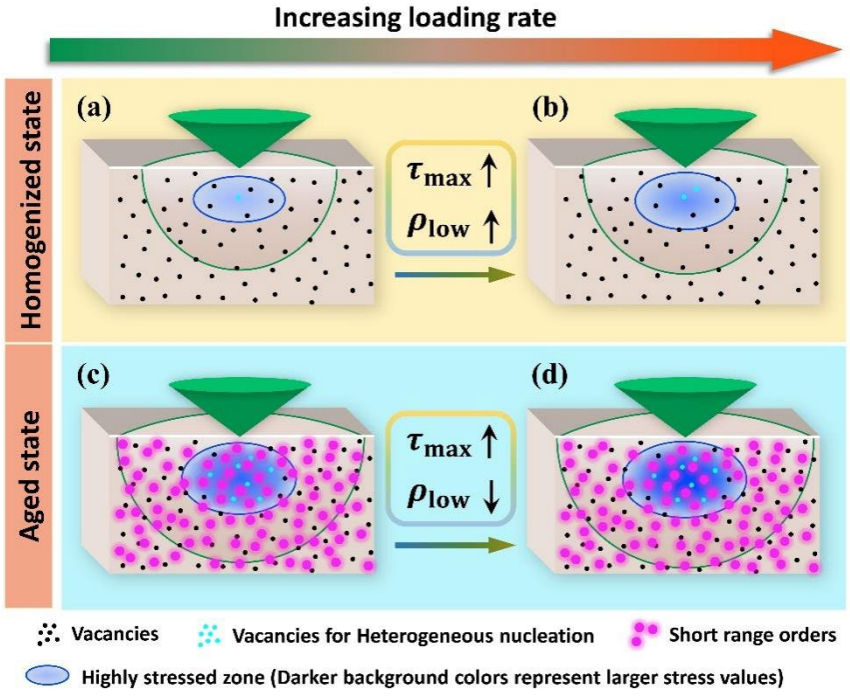

Fig. 4. Schematic illustration of the effect of SROs and loading rate on the dislocation-nucleation modes.